Emergent quantum transport due to quenched magnetic impurity scattering by antiferromagnetic proximity in $SrCuO_2/SrIrO_3$

Subhadip Jana,[1,2,*] T. Senapati,[2,3] Shwetha G. Bhat,[4] S. N. Sarangi,[1] K. Senapati,[2,3] and D. Samal[1,2,†]

[1]*Institute of Physics, Bhubaneswar 751005, India*

[2]*Homi Bhabha National Institute, Anushakti Nagar, Mumbai 400094, India*

[3]*School of Physical Sciences, National Institute of Science Education and Research, Bhubaneswar 752050, India*

[4]*Department of Physics, Indian Institute of Science, Bangalore 560012, India*

(Received 3 March 2022; revised 23 March 2023; accepted 28 March 2023; published 12 April 2023)

Through an antiferromagnetic proximity effect, we demonstrate the evidence for quenched magnetic impurity scattering in a spin-orbit-coupled semimetal $SrIrO_3$ proximitized with an antiferromagnetic $SrCuO_2$ layer from quantum interference originated magnetoconductance study. Two distinct observations, i.e., (i) enhanced effective phase coherence length (l_ϕ) and (ii) emergence of chiral-anomaly-induced topological response in longitudinal magnetoconductance ($\vec{B}||\vec{E}$), signify that the magnetic impurity scattering is suppressed in the $SrCuO_2/SrIrO_3$ bilayer. The quenching of magnetic impurity scattering is discussed in the framework of the antiferromagnetic proximity effect, which is originated from spin Andreev reflection at the $SrCuO_2/SrIrO_3$ interface. This work unfolds a practical means to circumvent the detrimental effect of unintended magnetic impurity scattering and preserve quantum phenomena in complex materials.

DOI: 10.1103/PhysRevB.107.134415

Interface effects in thin-film heterostructures provide opportunities to harness technologically relevant functionality and explore a wide range of remarkable phenomena which is not attainable in the constituent bulk counterparts. Striking examples include exchange bias at the ferromagnet/antiferromagnet interface [1–3], two-dimensional (2D) electron gas at an interface between two complex oxide band insulators [4], and various proximity effects (superconducting [5–7], magnetic [8–10], and topological [11–13]) through which a given material acquires properties of its adjacent layers across the interface.

In recent days, layered 5*d* transition-metal oxides such as iridates with their large spin-orbit coupling have emerged to host several spin-orbit-coupled quantum states [14–17] and open the possibility to explore novel proximity and dimensional effects in the iridate-based heterostructures [18–23]. Among iridates, orthorhombic perovskite $SrIrO_3$ (SIO) has gained significant attention because of its nontrivial band structure and semimetallic ground state, where the protected 3D Dirac node emerges from the combination of crystalline symmetry and spin-orbit interaction [24–27]. An angle-resolved photoemission spectroscopy (ARPES) study on SIO thin films revealed a steep linear electronic dispersion in the vicinity of Fermi energy, indicating the possibility to have Dirac fermions [28]. However, the evidence for the Dirac semimetallic response still remains elusive from the magneto-transport study.

The manifestation of quantum phenomena in electronic transport is influenced by different types of microscopic scattering processes. In particular, magnetic impurity scattering suppresses the quantum effects, e.g., weakens conventional superconductivity [29,30], drives the system from a quantum interference dominated effect [weak localization (WL) or weak antilocalization (WAL)] to a Drude-like scenario [31], and transforms a topological insulator to a topological trivial dilute magnetic semiconductor [32]. In real materials, magnetic impurity can arise due to the presence of unintended magnetic elements or from nonbonded defect atoms such as oxygen and, in most cases, it is unavoidable [33–35]. However, it was possible to suppress the unintended magnetic impurity scattering in Cu thin film through the proximity effect between a normal metal (Cu) and antiferromagnetic (AF) insulator (CuO) [36]. The theoretical work on the basis of spin Andreev reflection predicted that the proximity effect of antiferromagnetism in metal is ubiquitous at the metal/antiferromagnetic insulator interface [37], and, as a result, the spin-flip scattering of itinerant electrons by magnetic impurity becomes energetically unfavorable [36]. Taking advantage of the AF proximity effect that suppresses the undesired magnetic impurity scattering, we unravel the Dirac semimetallic topological response in SIO from a magnetoconductance study.

In this paper, we report the antiferromagnetic (infinite layer $SrCuO_2$ (SCO) [38–40]) proximity effect on the electron transport properties of $SrIrO_3$ in a $SrCuO_2/SrIrO_3$ bilayer. From the analysis of the low-temperature magnetoconductance data based on the theory of weak antilocalization, we find an enhanced effective phase coherence length (l_ϕ) in the SCO/SIO bilayer as compared to bare SIO film and this effect is attributed to the quenching of magnetic impurity scattering by a proximity effect of antiferromagnetism in the SIO layer. Remarkably, the SCO/SIO bilayer manifests positive longitu-

*subhadip.j@iopb.res.in

†dsamal@iopb.res.in

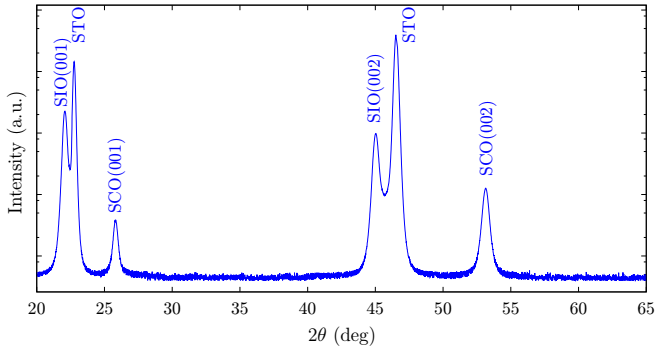

FIG. 1. θ-2θ x-ray diffraction pattern of the $SrCuO_2/SrIrO_3$ (∼14 nm/∼16 nm) bilayer film on a $SrTiO_3$ (0 0 1) substrate. The Y axis is in logarithmic scale.

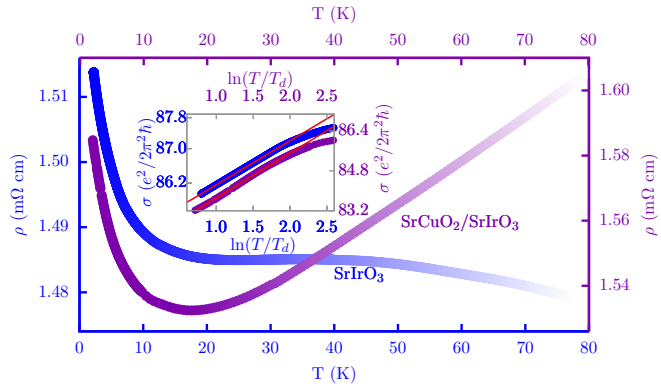

FIG. 2. Resistivity $\rho(T)$ vs T plot for $SrIrO_3$ (16 nm) (blue color) and $SrCuO_2/SrIrO_3$ (14/16 nm) (violet color) films. Inset: Quantum interference and *e-e* correlation originated sheet conductance $\sigma(T) \propto \ln(T)$ with $T_d = 1$ K [44] (solid red lines represent fitting).

dinal magnetoconductance (LMC) in the $(\vec{B}||\vec{E})$ configuration, in contrast to a bare SIO film. Positive LMC is one of the fingerprints of the Dirac/Weyl semimetallic response and it arises from a chiral-anomaly-induced axial charge current. The results indicate that the axial current is preserved in the SCO/SIO bilayer due to quenched magnetic impurity scattering, which otherwise is susceptible to random magnetic scattering.

SIO and SCO/SIO bilayer thin films are fabricated on (001)-oriented $SrTiO_3$ substrates by pulsed laser (Excimer laser KrF with (λ) = 248 nm) deposition (using a commercial polycrystalline SIO target having traces of Cr and Fe impurities [41]). A laser fluence 2 J/cm^2 and pulse rate of 1 Hz were used to ablate polycrystalline $SrIrO_3$ and $SrCuO_2$ targets to prepare the desired thin films. The substrate temperature was set at 650 °C for the growth of both $SrIrO_3$ and $SrCuO_2$ thin films. The oxygen partial pressure (P_{O_2}) of 0.2 mbar was maintained during deposition.

The structural characterization of the films are characterized by using x-ray diffraction with Cu-K_α radiation. Figure 1 shows the x-ray diffraction θ-2θ pattern for a $SrCuO_2/SrIrO_3$ bilayer that reveals only the characteristic (00l) Bragg's reflection of $SrIrO_3$ and $SrCuO_2$ indicating c-axis oriented growth. The electronic transport properties of orthorhombic $SrIrO_3$ thin films are sensitive to its structural distortion. Therefore, it was necessary to examine the crystal structure of the $SrIrO_3$ layer when directly grown on $SrTiO_3$ ($SrTiO_3/SrIrO_3$) and on the $SrCuO_2$ underlayer ($SrTiO_3/SrCuO_2/SrIrO_3$). In this regard, we have performed reciprocal space mapping (RSM) about the four equally spaced (103) planes of $SrTiO_3$ on both $SrTiO_3/SrIrO_3$ and $SrTiO_3/SrCuO_2/SrIrO_3$ thin films (shown in the Supplemental Material [42]). From RSM, we observe similar (Q_x, Q_y) values for the {103} set of planes corresponding to $SrIrO_3$ grown on $SrTiO_3/SrCuO_2$. This suggests an absence of distortion to the pseudocubic lattice structure of $SrIrO_3$ when grown on a nonperovskite $SrCuO_2$ layer. Similar observations are also made on $SrIrO_3$ thin film grown on $SrTiO_3$, indicating that $SrIrO_3$ has the same crystal structure, irrespective of its growth either on the $SrCuO_2$ underlayer ($SrTiO_3/SrCuO_2/SrIrO_3$) or directly on the $SrTiO_3$ substrate ($SrTiO_3/SrIrO_3$).

Figure 2 shows the temperature-dependent resistivity of SIO and SCO/SIO bilayer films. The thickness of the SIO layer in both cases is ∼16 nm, whereas the SCO thickness in the bilayer is ∼14 nm. The small resistivity variation (0.035 mΩ cm) over the measured temperature range (2–80 K) indicates the semimetallic ground state of SIO in overall agreement with the literature [19,43]. In the low-temperature regime, the resistivity shows an upturn below ∼15 K for both films, which can be attributed to quantum interference and electron-electron correlation effects. This is apparent from the linear $\ln(T)$ dependence on sheet conductance [$\sigma(T)$] below 8 K, as shown in the insets of Fig. 2.

To examine the effect of AF proximity on the microscopic electron scattering process in SIO, we have exploited a detailed analysis on the magnetotransport study based on quantum interference effects. Quantum interference originated correction to sheet conductance $\Delta\sigma(B_\perp)$ in the presence of a perpendicular magnetic field can be expressed by the Hikami-Larkin-Nagoka (HLN) equation [31,45,46] as

$$\Delta\sigma(B_\perp) = -\frac{e^2}{2\pi^2\hbar}\Bigg[\{\psi(1/2+B_e/B_\perp)+\ln(B_\perp/B_e)\} + \frac{1}{2}\{\psi(1/2+B_\phi/B_\perp)+\ln(B_\perp/B_\phi)\} - \frac{3}{2}\left\{\psi\left(1/2+\frac{B_\phi+B_{so}}{B_\perp}\right)+\ln\left(\frac{B_\perp}{B_\phi+B_{so}}\right)\right\}\Bigg], \quad (1)$$

where $\psi(x)$ is the digamma function, $B_\perp$ is the external magnetic field applied perpendicular to the film surface, and B_e, B_ϕ, and B_{so} are related with l_e, l_ϕ, and l_{so} as $B_i = \hbar/4el_i^2$, where l_e, l_ϕ and l_{so} denote elastic, phase coherence, and spin-orbit scattering lengths, respectively (B_e is determined using the semiclassical approximation utilizing conductivity and charge carrier density). Details are given in the Supplemental Material [42].

Figure 3(a) shows negative variation of the sheet conductance $\Delta\sigma(B_\perp)$ for SIO film at different temperatures. For the low magnetic field regime $B_\perp < B_{max}$ ($B_{max} = \hbar/4et^2 \sim 0.64\,T$, t is the thickness of the $SrIrO_3$ layer), a sharp

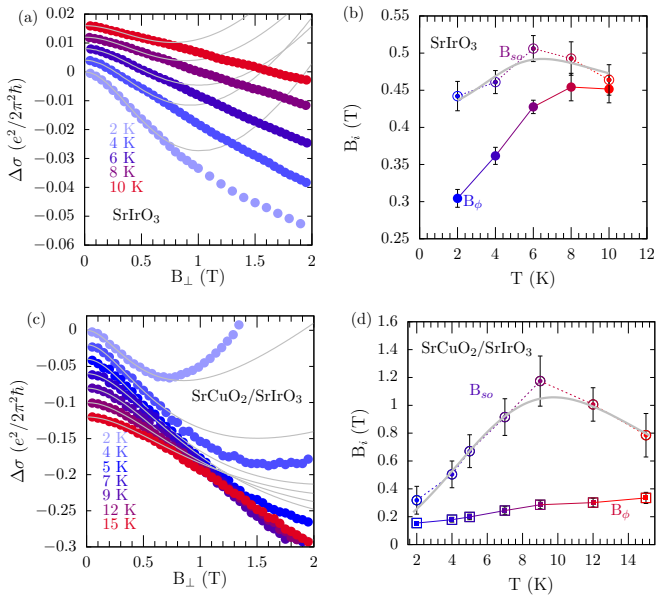

FIG. 3. Sheet conductance $\Delta\sigma(B_\perp)$ *vs* $B_\perp$ plot for (a) $SrIrO_3$ and (c) $SrCuO_2/SrIrO_3$ (vertical shift is given to data points for better clarity). Solid gray lines denote HLN fitting. The temperature dependence of B_ϕ, B_{so} are shown in (b),(d) for $SrIrO_3$ and $SrCuO_2/SrIrO_3$ films respectively. The solid gray line represents the fitting using generalized Elliott-Yafet type spin-relaxation (Eq. 2) and considering marginal Fermi-liquid behavior.

cusplike behavior is seen at low temperature (2–4 K), which is attributed to the WAL effect originating from strong spin-orbit interaction in SIO (Ir, Z = 77). As shown in Fig. 3(a), $\Delta\sigma(B_\perp)$ fits well with the HLN equation [Eq. (1)] in the low-field regime, and in the higher magnetic field regime $B_\perp > B_{\max}$, the HLN equation is not strictly valid.

The characteristic magnetic fields B_ϕ, B_{so} extracted from the fitting are shown in Fig. 3(b). It is found that $B_\phi(\propto l_\phi^{-2})$ rises upon increment of temperature and this is expected as l_ϕ gets reduced by random thermal agitation. B_{so} also exhibits a weakly temperature-dependent nonmonotonic behavior [Fig. 3(b)] and is unlike the usual cases where the characteristic spin-orbit magnetic field B_{so} is practically independent of temperature [36,47–49].

Considering the Elliott-Yafet (EY) type of spin-orbit scattering to be dominant in SIO because of the presence of bulk inversion symmetry [50], the expression for τ_{so} is given as [51]

$$\frac{1}{\tau_{so}} = \frac{\lambda_{so}^2}{\hbar^2}\frac{\tau_e}{\left(1+\Delta\omega_{\text{eff}}^2\tau_e^2\right)}, \tag{2}$$

where, λ_{so} and ω_{eff} represent the effective atomic spin-orbit-coupling strength and equivalent frequency ($\Delta E = \hbar\Delta\omega_{\text{eff}}$) of energy separation ($\Delta E$) between the valence and conduction bands in the vicinity of Fermi energy (E_F), respectively. At low temperature, the charge dynamics in SIO exhibits marginal Fermi-liquid behavior and the quasiparticle relaxation time (τ_e) follows $\tau_e \propto (T/\ln\frac{\omega}{T})^{-1}$, where ω is the cutoff frequency related to the bandwidth [52]. Substituting the expression for τ_e in the generalized EY equation [Eq. (2)], it is possible to account for the observed anomalous feature of B_{so} vs T [fitting shown in Fig. 3(b)].

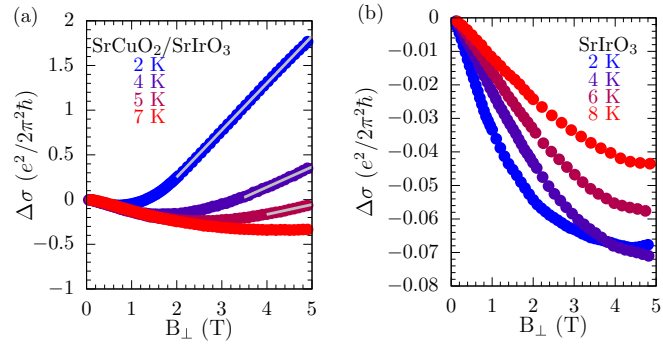

FIG. 4. $\Delta\sigma(B_\perp)$ vs $B_\perp$ plots for (a) $SrCuO_2/SrIrO_3$ and (b) $SrIrO_3$ films. At low temperature (2–5 K) and high magnetic field, MC increases linearly with B for the $SrCuO_2/SrIrO_3$ bilayer (linear fittings are denoted by solid gray line).

For the SCO/SIO bilayer, $\Delta\sigma(B_\perp)$ vs $B_\perp$ plots are illustrated in Fig. 3(c) and it reveals that WAL sustains up to a relatively higher temperature (∼15 K). Furthermore, the extracted B_ϕ for SCO/SIO is less than that of SIO and does not saturate even up to 15 K. In the presence of weak magnetic impurity scattering (unintentional Fe, Cr elements and possible oxygen vacancy at the interface), the effective l_ϕ is determined by $l_\phi^{-2} = l_{\phi\,\text{ideal}}^{-2} + l_m^{-2}$, where l_m is the magnetic impurity scattering length [53]. The observation of a relatively small (large) value of B_ϕ (l_ϕ) indicates that the effective magnetic impurity scattering is weaker in SCO/SIO. This effect is attributed to the quenching of magnetic impurity scattering by the AF proximity effect resulting from spin Andreev reflection [37]. The induced AF spin polarization of itinerant electrons in the metallic side makes the spin-flip scattering by magnetic impurity energetically unfavorable, i.e., magnetic impurity scattering is effectively quenched [36]. Usually magnetic impurity breaks time-reversal symmetry and drives the system to a classical limit from the WL/WAL limit [31,54–57]. Since magnetic impurity scattering is suppressed in SCO/SIO, WAL manifests up to a higher temperature.

Particularly in SCO/SIO, B_{so} vs T exhibits a prominent variation and is fitted [Fig. 3(d)] by considering EY-type spin-orbit scattering [Eq. (2)]. The prominent variation in B_{so} can be assimilated by invoking a stronger marginal Fermi-liquid behavior in SIO when it is proximitized with AF. It is consistent with the theoretical predication that the antiferromagnet tends to drive a correlated system from conventional Fermi liquid to marginal Fermi liquid [58].

Figure 4 shows the variation of $\Delta\sigma(B_\perp)$ for SCO/SIO and SIO films up to an extended field range of 5 T. In the presence of strong spin-orbit scattering, quantum interference originated correction to conductance [$\Delta\sigma(B_\perp)$] is negative in the low magnetic field (WAL effect). However, the quantum correction to magnetoconductance (MC) can be positive at a higher magnetic field when $eB\tau_e/m^* > 1/\hbar E_F\tau_{so}$, where τ_e, τ_{so}, m^*, and E_F are the momentum scattering time, spin-orbit scattering time, effective mass, and Fermi energy, respectively [59]. If this happens to be the case, then both systems (SCO/SIO, SIO) should have shown positive $\Delta\sigma(B_\perp)$ at a higher magnetic field. But, we observe positive $\Delta\sigma(B_\perp)$ for SCO/SIO, which is intriguing. In the quantum diffusive

regime, conductivity in a weakly disordered system is related to the current-current correlation (Kubo formula). Based on this formalism, the conductance at low temperature for a Dirac semimetal with an applied transverse magnetic field is given by [60]

$$\sigma \propto \frac{\gamma \Omega^2}{v_F^4} + \bigcirc\left(\frac{\gamma^2 \Omega^3}{v_F^4}\right), \tag{3}$$

where γ is a randomly distributed scattering potential correlator, $\Omega = v_F\sqrt{2eB}$, and $\bigcirc$ denotes higher order. For the pointlike neutral scattering potential, γ is independent of B, and hence $\sigma \propto B$ [neglecting the higher-order term in Eq. (3) as $\gamma << 1$ for weak disorder]. On the contrary, the long-range screening potential [$U(k) \propto 1/(k^n + \lambda)$, where λ is the inverse screening length] leads to explicit magnetic field dependent γ ($\gamma \propto B^{-n}$) and, as a result, $\sigma \propto B^{-n+1}$ [61]. We therefore hypothesize that the observed positive linear MC is an indication of Dirac electronic behavior in SCO/SIO, where the quenched magnetic impurity effectively acts as a pointlike neutral scattering potential. This is unlike the case for a bare SIO film that experiences a long-range screening magnetic potential and exhibits negative MC.

To further augment the finding of a Dirac-like electronic response, we have performed longitudinal magnetoconductance (LMC) in parallel magnetic and electric fields ($\vec{B}||\vec{E}$). It is found that SCO/SIO exhibits positive LMC at a higher magnetic field [Fig. 5(a)], whereas the same for SIO is negative [Fig. 5(b)] across the measured magnetic field range. The observed positive LMC in SCO/SIO with the $\vec{B}||\vec{E}$ configuration is quite nontrivial and inconsistent with the classical origin. However, it can be a consequence of Adler-Bell-Jackiw chiral anomaly.

In a topological Dirac semimetal, the external magnetic field ($\vec{B}$) can split each Dirac node into two Weyl nodes with opposite chirality in momentum space along the applied field. The current driving external electric field ($\vec{E}$) in parallel $\vec{B}$ pumps more electrons around one Weyl node compared to another with opposite chirality [illustrated in Fig. 5(c)] [62–66]. This gives rise to chiral charge imbalance resulting in an axial current; as a consequence, $\Delta\sigma(B_{||})$ increases with $B_{||}$ and follows a quadratic functional dependence. The variation of $\Delta\sigma(B_{||})$ at different temperatures is fitted with $C_w B_{||}^2 + a\ln(B_{||})$ [Fig. 5(a)] at a higher magnetic field regime, where C_w stands for the chiral anomaly originated correction (the $a \ln B_{||}$ term accounts for quantum interference correction to conductance in a parallel magnetic field configuration). The temperature dependence of chiral anomaly originated conductance $\Delta\sigma_{\text{chiral}}(B_{||}, T)$ can be expressed as

$$\Delta\sigma_{\text{chiral}}(B_{||}, T) = \frac{3e^4 v_F^3}{8\pi^4\hbar^2 c}\frac{\tau_a}{T^2 + (\mu/\pi)^2}B_{||}^2 = C_w B_{||}^2, \tag{4}$$

where μ is the chemical potential [67,68]. The quadratic dependence of C_w on T is reflected in the fitting [inset of Fig. 5(a)].

The observed contrasting trend of LMC in SIO and SCO/SIO [Figs. 5(a) and 5(b)] can be elucidated as follows. In the presence of considerable magnetic impurity scattering in SIO, the characteristic chiral relaxation time (τ_a) gets reduced (as magnetic impurity breaks chirality [69]), and hence the chirality originated conductance is suppressed. In such scenario, the classical contribution to negative $\Delta\sigma(B)$ dominates and the system can exhibit negative longitudinal MC [70,71]. On the contrary, the reverse effect occurs in SCO/SIO, where quenched magnetic impurity scattering leads to increased τ_a. With the application of an electric field, the chiral charge imbalance increases as it is proportional to $\tau_a E$, and generates chiral current.

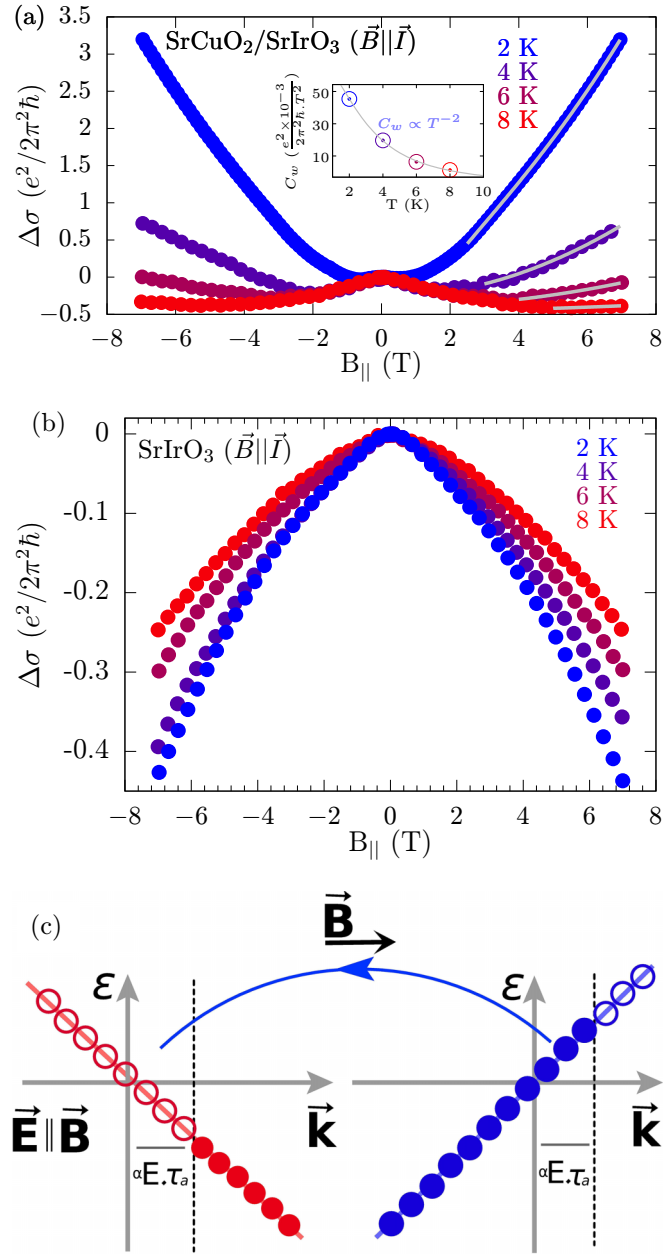

FIG. 5. (a) $\Delta\sigma(B_{||})$ vs $B_{||}$ plot for $SrCuO_2/SrIrO_3$. $\Delta\sigma$ is fitted well with $C_w B_{||}^2 + a\ln(B_{||})$ and shown with a gray line. Inset: Temperature variation of $C_w(T) \propto T^{-2}$ [Eq. (4)]. (b) The $SrIrO_3$ film exhibits negative longitudinal magnetoconductance. (c) The schematic illustration of axial current (light-blue arrow) due to chiral charge imbalance ($\propto E\,\tau_a$) in $SrCuO_2/SrIrO_3$. The filled (empty) circles represent occupied (empty) states. Blue and red indicate opposite chirality.

Importantly, chiral anomaly is not the only effect that gives rise to the positive LMC [72,73]. It may also originate from nonchiral effects which are not associated with the intrinsic material property. Here, we have discussed the other possibilities and their relevance to our study. Positive LMC may originate through the current jetting effect [74,75]. Had that been the case, both SIO and SCO/SIO should have similarly shown positive LMC (note that the lead connection to the samples was made by the wire bonder and these were almost identical in both cases). However, we observe a complete trend reversal. Second, since current jetting is a geometrical effect, the induced positive LMC cannot disappear sharply with increment of temperature as we observe in the case of SCO/SIO film [76]. It is also possible to observe positive LMC in a quasi-two-dimensional metal possessing a corrugated single-sheet Fermi surface (such as $PdCoO_2$) [77], but this is not relevant in the context of perovskite SIO.

We have presented an extensive magnetotransport study of spin-orbit-coupled semimetallic $SrIrO_3$ thin film and a bilayer system in which $SrIrO_3$ is proximitized with a $SrCuO_2$ antiferromagnet Mott insulator. From the analysis of low-temperature magnetoconductance data based on the quantum interference effect, we find an enhanced effective phase coherence length (l_ϕ) in the $SrCuO_2/SrIrO_3$ bilayer as compared to $SrIrO_3$. This is ascribed to quenched magnetic impurity scattering in $SrIrO_3$ by the antiferromagnetic proximity effect. Further, in the $\vec{B}||\vec{E}$ configuration, longitudinal magnetoconductance measurements reveal a topological Dirac semimetallic response in $SrCuO_2/SrIrO_3$, which is absent in $SrIrO_3$. The antiferromagnetic proximity effect thus paves an avenue to preserve the nontrivial quantum phenomena in real complex materials by circumventing the detrimental effect of unintended magnetic impurity scattering. From a spintronics technological point of view, it will also be useful as an effective way to control undesired spin relaxation by magnetic impurity scattering.

S.J. and D.S. acknowledge the financial support from the Max Planck partner group. D.S. thanks SERB, Govt. of India for research grant (Grant No. CRG/Z019/005144). S.G.B. acknowledges DST INSPIRE Faculty Fellowship for the financial assistance. T.S. and K.S. acknowledge the funding from National Institute of Science Education and Research (NISER), HBNI, Department of atomic energy (DAE), India, through plan project "RIN-4001".

[1] W. H. Meiklejohn and C. P. Bean, Phys. Rev. **105**, 904 (1957).
[2] J. Nogues and I. K. Schuller, J. Magn. Magn. Mater. **192**, 203 (1999).
[3] B. C. Behera, S. Jana, S. G. Bhat, N. Gauquelin, G. Tripathy, P. S. Anil Kumar, and D. Samal, Phys. Rev. B **99**, 024425 (2019).
[4] A. Ohtomo and H. Hwang, Nature (London) **427**, 423 (2004).
[5] H. Meissner, Phys. Rev. **117**, 672 (1960).
[6] P. G. de Gennes, Rev. Mod. Phys. **36**, 225 (1964).
[7] A. I. Buzdin, Rev. Mod. Phys. **77**, 935 (2005).
[8] F. Hellman, A. Hoffmann, Y. Tserkovnyak, G. S. D. Beach, E. E. Fullerton, C. Leighton, A. H. MacDonald, D. C. Ralph, D. A. Arena, H. A. Durr *et al.*, Rev. Mod. Phys. **89**, 025006 (2017).
[9] B. Huang, M. A. McGuire, A. F. May, D. Xiao, P. Jarillo-Herrero, and X. Xu, Nat. Mater. **19**, 1276 (2020).
[10] J. Matsuno, N. Ogawa, K. Yasuda, F. Kagawa, W. Koshibae, N. Nagaosa, Y. Tokura, and M. Kawasaki, Sci. Adv. **2**, 1600304 (2016).
[11] T. H. Hsieh, H. Ishizuka, L. Balents, and T. L. Hughes, Phys. Rev. Lett. **116**, 086802 (2016).
[12] C. Trang, N. Shimamura, K. Nakayama, S. Souma, K. Sugawara, I. Watanabe, K. Yamauchi, T. Oguchi, K. Segawa, T. Takahashi *et al.*, Nat. Commun. **11**, 159 (2020).
[13] T. Shoman, A. Takayama, T. Sato, S. Souma, T. Takahashi, T. Oguchi, K. Segawa, and Y. Ando, Nat. Commun. **6**, 1 (2015).
[14] J. G. Rau, E. K.-H. Lee, and H.-Y. Kee, Annu. Rev. Condens. Matter Phys. **7**, 195 (2016).
[15] B. J. Kim, H. Jin, S. J. Moon, J.-Y. Kim, B.-G. Park, C. S. Leem, J. Yu, T. W. Noh, C. Kim, S.-J. Oh, J.-H. Park, V. Durairaj, G. Cao, and E. Rotenberg, Phys. Rev. Lett. **101**, 076402 (2008).
[16] S. J. Moon, H. Jin, K. W. Kim, W. S. Choi, Y. S. Lee, J. Yu, G. Cao, A. Sumi, H. Funakubo, C. Bernhard, and T. W. Noh, Phys. Rev. Lett. **101**, 226402 (2008).
[17] Y. K. Kim, N. Sung, J. Denlinger, and B. Kim, Nat. Phys. **12**, 37 (2016).
[18] L. Hao, D. Meyers, M. Dean, and J. Liu, J. Phys. Chem. Solids **128**, 39 (2019).
[19] J. Matsuno, K. Ihara, S. Yamamura, H. Wadati, K. Ishii, V. V. Shankar, H.-Y. Kee, and H. Takagi, Phys. Rev. Lett. **114**, 247209 (2015).
[20] J. Nichols, X. Gao, S. Lee, T. L. Meyer, J. W. Freeland, V. Lauter, D. Yi, J. Liu, D. Haskel, J. R. Petrie *et al.*, Nat. Commun. **7**, 1 (2016).
[21] D. Yi, J. Liu, S.-L. Hsu, L. Zhang, Y. Choi, J.-W. Kim, Z. Chen, J. D. Clarkson, C. R. Serrao, E. Arenholz *et al.*, Proc. Natl. Acad. Sci. **113**, 6397 (2016).
[22] E. Skoropata, J. Nichols, J. M. Ok, R. V. Chopdekar, E. S. Choi, A. Rastogi, C. Sohn, X. Gao, S. Yoon, T. Farmer *et al.*, Sci. Adv. **6**, 3902 (2020).
[23] D. Yi, C. L. Flint, P. P. Balakrishnan, K. Mahalingam, B. Urwin, A. Vailionis, A. T. NDiaye, P. Shafer, E. Arenholz, Y. Choi, K. H. Stone, J. H. Chu, B. M. Howe, J. Liu, I. R. Fisher, and Y. Suzuki, Phys. Rev. Lett. **119**, 077201 (2017).
[24] Y. Chen, Y.-M. Lu, and H.-Y. Kee, Nat. Commun. **6**, 6593 (2015).
[25] J.-M. Carter, V. V. Shankar, M. A. Zeb, and H.-Y. Kee, Phys. Rev. B **85**, 115105 (2012).
[26] M. A. Zeb and H.-Y. Kee, Phys. Rev. B **86**, 085149 (2012).
[27] H.-S. Kim, Y. Chen, and H.-Y. Kee, Phys. Rev. B **91**, 235103 (2015).
[28] Y. F. Nie, P. D. C. King, C. H. Kim, M. Uchida, H. I. Wei, B. D. Faeth, J. P. Ruf, J. P. C. Ruff, L. Xie, X. Pan, C. J. Fennie, D. G. Schlom, and K. M. Shen, Phys. Rev. Lett. **114**, 016401 (2015).
[29] P. W. Anderson, J. Phys. Chem. Solids **11**, 26 (1959).
[30] A. V. Balatsky, I. Vekhter, and J.-X. Zhu, Rev. Mod. Phys. **78**, 373 (2006).

[31] S. Hikami, A. I. Larkin, and Y. Nagaoka, Prog. Theor. Phys. **63**, 707 (1980).

[32] M. Liu, J. Zhang, C.-Z. Chang, Z. Zhang, X. Feng, K. Li, K. He, L.-l. Wang, X. Chen, X. Dai, Z. Fang, Q.-K. Xue, X. Ma, and Y. Wang, Phys. Rev. Lett. **108**, 036805 (2012).

[33] A. Brinkman, M. Huijben, M. Van Zalk, J. Huijben, U. Zeitler, J. Maan, W. G. van der Wiel, G. Rijnders, D. H. Blank, and H. Hilgenkamp, Nat. Mater. **6**, 493 (2007).

[34] L. Li, C. Richter, J. Mannhart, and R. Ashoori, Nat. Phys. **7**, 762 (2011).

[35] B. W. Veal, S. K. Kim, P. Zapol, H. Iddir, P. M. Baldo, and J. A. Eastman, Nat. Commun. **7**, 1 (2016).

[36] K. Munakata, T. H. Geballe, and M. R. Beasley, Phys. Rev. B **84**, 161405(R) (2011).

[37] K. A. Al-Hassanieh, J. Rincón, G. Alvarez, and E. Dagotto, Phys. Rev. Lett. **114**, 066401 (2015).

[38] D. Samal, H. Tan, H. Molegraaf, B. Kuiper, W. Siemons, S. Bals, J. Verbeeck, G. Van Tendeloo, Y. Takamura, E. Arenholz, C. A. Jenkins, G. Rijnders, and G. Koster, Phys. Rev. Lett. **111**, 096102 (2013).

[39] M. Dantz, J. Pelliciari, D. Samal, V. Bisogni, Y. Huang, P. Olalde-Velasco, V. Strocov, G. Koster, and T. Schmitt, Sci. Rep. **6**, 32896 (2016).

[40] K. Mikhalev, S. Verkhovskii, A. Gerashenko, A. Mirmelstein, V. Bobrovskii, K. Kumagai, Y. Furukawa, T. D'yachkova, and Y. Zainulin, Phys. Rev. B **69**, 132415 (2004).

[41] The magnetic impurity in used target: Cr $<$ 0.002 (wt %), Fe $<$ 0.002 (wt %).

[42] See Supplemental Material at http://link.aps.org/supplemental/10.1103/PhysRevB.107.134415 for reciprocal space mappingand determining B_e.

[43] A. Biswas, K.-S. Kim, and Y. H. Jeong, J. Appl. Phys. **116**, 213704 (2014).

[44] Function $\ln(x)$ is not defined for dimensioned quantities. Therefore, to make the argument dimensionless, we use $\ln(T/T_d)$ as the x-axis label of the inset of Fig. 2 with $T_d = 1$K.

[45] S. Jana, S. G. Bhat, B. C. Behera, L. Patra, P. S. A. Kumar, B. R. K. Nanda, and D. Samal, Europhys. Lett. **133**, 17005 (2021).

[46] S. Jana, T. Senapati, and D. Samal, Phys. Rev. B **103**, 245109 (2021).

[47] N. P. Breznay, H. Volker, A. Palevski, R. Mazzarello, A. Kapitulnik, and M. Wuttig, Phys. Rev. B **86**, 205302 (2012).

[48] I. Zutic, J. Fabian, and S. Das Sarma, Rev. Mod. Phys. **76**, 323 (2004).

[49] S. Jana, T. Senapati, K. Senapati, and D. Samal, Phys. Rev. B **107**, 035127 (2023).

[50] R. J. Elliott, Phys. Rev. **96**, 266 (1954).

[51] F. Simon, B. Dora, F. Murányi, A. Jánossy, S. Garaj, L. Forro, S. Bud'ko, C. Petrovic, and P. C. Canfield, Phys. Rev. Lett. **101**, 177003 (2008).

[52] K. Sen, D. Fuchs, R. Heid, K. Kleindienst, K. Wolff, J. Schmalian, and M. Le Tacon, Nat. Commun. **11**, 1 (2020).

[53] B. Al'Tshuler, A. Aronov, A. Larkin, and D. Khmel'Nitskii, Zh. Eksp. Teor. Fiz. **81**, 768 (1981) [Sov. Phys. JETP 54, 411 (1981)].

[54] H. Beckmann and G. Bergmann, Phys. Rev. B **54**, 368 (1996).

[55] H. Beckmann, R. Schüfer, W. Li, and G. Bergmann, Europhys. Lett. **33**, 563 (1996).

[56] H. Beckmann and G. Bergmann, J. Low Temp. Phys. **110**, 1173 (1998).

[57] G. Bergmann, Intl. J. Mod. Phys. B **24**, 2015 (2010).

[58] G. T. Zimanyi and K. S. Bedell, Phys. Rev. B **48**, 6575 (1993).

[59] B. Al'Tshuler and A. Aronov, Pis'ma Zh. Eskp. Teor. Fiz. **33**, 515 (1981) [JETP Lett. **33**, 499 (1981)].

[60] J. Klier, I. V. Gornyi, and A. D. Mirlin, Phys. Rev. B **92**, 205113 (2015).

[61] Y. I. Rodionov, K. I. Kugel, B. A. Aronzon, and F. Nori, Phys. Rev. B **102**, 205105 (2020).

[62] J. Xiong, S. K. Kushwaha, T. Liang, J. W. Krizan, M. Hirschberger, W. Wang, R. J. Cava, and N. P. Ong, Science **350**, 413 (2015).

[63] A. Burkov, Nat. Mater. **15**, 1145 (2016).

[64] M.-X. Deng, W. Luo, R.-Q. Wang, L. Sheng, and D. Y. Xing, Phys. Rev. B **96**, 155141 (2017).

[65] E. V. Gorbar, V. A. Miransky, and I. A. Shovkovy, Phys. Rev. B **88**, 165105 (2013).

[66] The eigenstate (vector field) of the Dirac Hamilton can be identified with helicity, and in the case of a Weyl, the same will be chiralty. Helicity and chirality are the same for massless quasiparticles, but are not valid for general cases.

[67] K. Fukushima, D. E. Kharzeev, and H. J. Warringa, Phys. Rev. D **78**, 074033 (2008).

[68] Q. Li, D. E. Kharzeev, C. Zhang, Y. Huang, I. Pletikosic, A. Fedorov, R. Zhong, J. Schneeloch, G. Gu, and T. Valla, Nat. Phys. **12**, 550 (2016).

[69] B. Fu, H.-W. Wang, and S.-Q. Shen, Phys. Rev. B **101**, 125203 (2020).

[70] D. T. Son and B. Z. Spivak, Phys. Rev. B **88**, 104412 (2013).

[71] A. A. Burkov, Phys. Rev. Lett. **113**, 247203 (2014).

[72] C.-L. Zhang, S.-Y. Xu, I. Belopolski, Z. Yuan, Z. Lin, B. Tong, G. Bian, N. Alidoust, C.-C. Lee, S.-M. Huang *et al.*, Nat. Commun. **7**, 10735 (2016).

[73] S. Jia, S.-Y. Xu, and M. Z. Hasan, Nat. Mater. **15**, 1140 (2016).

[74] A. B. Pippard, *Magnetoresistance in Metals* (Cambridge University Press, Cambridge, 1989), Vol. 2.

[75] S. Liang, J. Lin, S. Kushwaha, J. Xing, N. Ni, R. J. Cava, and N. P. Ong, Phys. Rev. X **8**, 031002 (2018).

[76] J. Hu, T. F. Rosenbaum, and J. B. Betts, Phys. Rev. Lett. **95**, 186603 (2005).

[77] N. Kikugawa, P. Goswami, A. Kiswandhi, E. Choi, D. Graf, R. Baumbach, J. Brooks, K. Sugii, Y. Iida, M. Nishio *et al.*, Nat. Commun. **7**, 1 (2016).